



Observations of Field Current and Field Winding Temperature in Electrically Excited Synchronous Machines with Brushless Excitation

Downloaded from: <https://research.chalmers.se>, 2025-12-04 22:44 UTC

Citation for the original published paper (version of record):

Tang, J., Jiang, B., Boscaglia, L. et al (2022). Observations of Field Current and Field Winding Temperature in Electrically Excited Synchronous Machines with Brushless Excitation. 2022 International Conference on Electrical Machines, ICEM 2022: 841-847. <http://dx.doi.org/10.1109/ICEM51905.2022.9910595>

N.B. When citing this work, cite the original published paper.

Observations of Field Current and Field Winding Temperature in Electrically Excited Synchronous Machines with Brushless Excitation

Junfei Tang, *Member, IEEE*, Bowen Jiang, *Student Member, IEEE*,

Luca Boscaglia, *Student Member, IEEE*, Hao Chen, *Member, IEEE*, and Yujing Liu, *Senior Member, IEEE*

Abstract -- Electrically excited synchronous machines have become an alternative in electrification of transportations and renewable power generations. To reduce the extra effort in the maintenance of sliprings and brushes for field excitation, brushless excitation has been developed. However, when brushless excitation is adopted, the field winding becomes physically inaccessible when the machine is rotating. To solve this problem, an algorithm is proposed in this study to observe the field current and field winding temperature of an EESM with brushless excitation. The stator currents are measured and then used to correct the machine state predictor. The correction of the state prediction is interpreted to adjust the field winding resistance and temperature value. The algorithm is evaluated in simulations. The estimations of field current and field winding temperature track the measurements successfully.

Index Terms—Electric machine control, electrically excited synchronous machine

I. INTRODUCTION

ELECTRICALLY excited synchronous machines (EESM) have become an alternative to permanent magnet synchronous machines (PMSM) in electric vehicles (EV) [1] [2]. EESMs have been equipped in BMW i4 and BMW iX and have been used as a highly efficient magnet-free electric motor in MAHLE [3] [4] [5]. The prevalence of EESMs is mainly due to two reasons. One reason is that rare earth materials are not used in an EESM. This means that the materials needed to construct an EESM are easy to access and the technology to recycle the machine is mature [6] [7] [8]. The second reason is that the excitation level of an EESM is adjustable [9] [10] [11] [12] [13]. The adjustable excitation level means a higher field current can be applied at

low speed to achieve a higher acceleration torque, while using the same machine at high speed, the field current can be reduced so that the copper and iron core losses can be reduced. In addition, with an adjustable field current, unity power factor can be realized at peak power, so that a higher output active power can be achieved.

Apart from the aforementioned advantages, introducing the technology of brushless excitation has made the application of EESMs more promising. With brushless excitation, the extra effort to clean the sliprings and brushes of the field excitation system are saved. In addition, the friction losses due to the contact of brushes and sliprings are eliminated. There are mainly two categories of brushless excitation, the inductive one used in [14] and the capacitive one implemented in [15]. In either of the technologies, there are two sides of the brushless power transfer system. The primary side is standing still with the stator while the secondary side is connected to the field winding in the rotor. In the inductive topology, a rotating transformer is employed, whereas in the capacitive topology, rotary plates are sandwiched between stationary plates with large surface and small airgap.

However, when brushless excitation is adopted, the field winding in the rotor becomes physically inaccessible when the machine is in operation. This leads to the problem of how to observe the field current for machine control and how to estimate the field winding temperature in case of overheat. A study of this topic is presented in [16]. An algorithm is proposed to observe the current and temperature of the field winding. The dc-link input current to the excitor is predicted and compared with the measurement. The error in between is then used to correct the estimations. The effectiveness of the algorithm is validated in experiments. However, there are two drawbacks of the algorithm. The tracking of field current and temperature relies on the efficiency profiles of the power electronic circuit in the excitation system. This means that each excitation system needs to be individually tested at different temperatures and different power levels before operation. Besides, an additional current sensor to measure the input dc-link current of the excitation converter is needed. These complicate the solution of a brushless EESM.

The aim of this study is therefore to investigate the possibility to observe the field current and field winding temperature using armature (stator) currents as the measurements to correct the estimation. In this study, a new type of observer is proposed to track the field current and field winding temperature. Electrical dynamics of an EESM

This project has received funding from the EU LONGRUN project under grant agreement No. 874972. The opinions expressed in this document reflect only the authors' view and reflect in no way the European Commission's opinions. The European Commission is not responsible for any use that may be made of the information it contains.

Junfei Tang is with Electric Power Engineering, Chalmers University of Technology, Gothenburg, Sweden (e-mail: junfei.tang@chalmers.se).

Bowen Jiang is with Electric Power Engineering, Chalmers University of Technology, Gothenburg, Sweden (bowen.jiang@chalmers.se).

Luca Boscaglia is with Electric Power Engineering, Chalmers University of Technology, Gothenburg, Sweden (luca.boscaglia@chalmers.se).

Hao Chen is with Electric Power Engineering, Chalmers University of Technology, Gothenburg, Sweden (hao.chen@chalmers.se).

Yujing Liu is with Electric Power Engineering, Chalmers University of Technology, Gothenburg, Sweden (yujing.liu@chalmers.se).

are modelled and the model is used to predict the currents in armature (stator) and field (rotor). The stator currents are measured and then compared to the predicted values of currents. The error in between is fed into a correction mechanism. A correction vector is then calculated to adjust the prediction. The correction vector is also interpreted to extract the error in field winding temperature estimation. The temperature estimation is adjusted accordingly to track the real temperature of the field winding.

In this article, firstly the electrical dynamics are modelled. Then based on the model, the current controller with decoupling of stator and field windings is introduced and the observer is presented. In the end, the performance of the observer is evaluated step by step in simulations.

II. MODELING OF EESM DYNAMICS

The electrical dynamics of an EESM describes the time-domain responses of d-axis, q-axis and field currents due to the applied d-axis, q-axis and field voltages across the electrical terminals of the machine. The speed of the machine is considered as given. The schematic diagram of EESM electrical dynamics is presented in Fig. 1.

A. Electrical Dynamics

The electrical dynamics of the machine can be described in matrix form as

$$\mathbf{u} = \mathbf{R}\mathbf{i} + \omega\boldsymbol{\psi} + \frac{d\boldsymbol{\psi}}{dt} \quad (1)$$

where \mathbf{u} , \mathbf{i} and $\boldsymbol{\psi}$ are the vectors of voltages, currents and flux linkages in d-axis, q-axis and field

$$\mathbf{u} = \begin{bmatrix} u_d \\ u_q \\ u_f \end{bmatrix}, \quad \mathbf{i} = \begin{bmatrix} i_d \\ i_q \\ i_f \end{bmatrix}, \quad \boldsymbol{\psi} = \begin{bmatrix} \psi_d \\ \psi_q \\ \psi_f \end{bmatrix} \quad (2)$$

\mathbf{R} and ω are the matrices of resistances and speed

$$\mathbf{R} = \begin{bmatrix} R_s & 0 & 0 \\ 0 & R_s & 0 \\ 0 & 0 & R_f \end{bmatrix}, \quad \omega = \begin{bmatrix} 0 & -\omega_r & 0 \\ \omega_r & 0 & 0 \\ 0 & 0 & 0 \end{bmatrix} \quad (3)$$

The flux linkage vector $\boldsymbol{\psi}$ can be further described as the multiplication of apparent inductance and current

$$\boldsymbol{\psi} = \mathbf{L}\mathbf{i} \quad (4)$$

where \mathbf{L} is the matrix of apparent inductances

$$\mathbf{L} = \begin{bmatrix} L_{dd} & L_{dq} & L_{df} \\ L_{qd} & L_{qq} & L_{qf} \\ L_{fd} & L_{fq} & L_{ff} \end{bmatrix} \quad (5)$$

The derivatives of flux linkages can be described as derivatives of currents

$$\frac{d\boldsymbol{\psi}}{dt} = \mathbf{l} \frac{d\mathbf{i}}{dt} \quad (6)$$

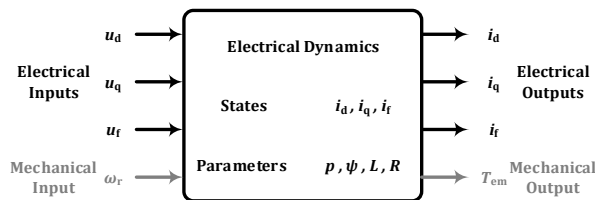


Fig. 1 Schematic diagram of EESM electrical dynamics.

where \mathbf{l} is the matrix of incremental inductances

$$\mathbf{l} = \begin{bmatrix} l_{dd} & l_{dq} & l_{df} \\ l_{qd} & l_{qq} & l_{qf} \\ l_{fd} & l_{fq} & l_{ff} \end{bmatrix} \quad (7)$$

Using apparent and incremental inductances, (1) can be reformulated as

$$\mathbf{u} = \mathbf{R}\mathbf{i} + \omega\mathbf{L}\mathbf{i} + \mathbf{l} \frac{d\mathbf{i}}{dt} \quad (8)$$

B. State Space Form

The current derivatives can be derived from electrical dynamics in (8)

$$\frac{d\mathbf{i}}{dt} = -\mathbf{l}^{-1}(\mathbf{R} + \omega\mathbf{L})\mathbf{i} + \mathbf{l}^{-1}\mathbf{u} \quad (9)$$

This can be formulated into the state space form

$$\frac{d\mathbf{i}}{dt} = \mathbf{A}\mathbf{i} + \mathbf{B}\mathbf{u} \quad (10)$$

where \mathbf{A} is the dynamic matrix

$$\mathbf{A} = -\mathbf{l}^{-1}(\mathbf{R} + \omega\mathbf{L}) \quad (11)$$

and \mathbf{B} is the control matrix

$$\mathbf{B} = \mathbf{l}^{-1} \quad (12)$$

The d- and q-axis stator currents are measured. Hence the output equation can be formulated as

$$\mathbf{y} = \mathbf{C}\mathbf{i} \quad (13)$$

where \mathbf{C} is the sensor matrix

$$\mathbf{y} = \begin{bmatrix} i_d \\ i_q \end{bmatrix}, \quad \mathbf{C} = \begin{bmatrix} 1 & 0 & 0 \\ 0 & 1 & 0 \end{bmatrix} \quad (14)$$

C. Implementation

The current vector \mathbf{i} is obtained from an integration of current derivatives $d\mathbf{i}/dt$, and the current derivatives are calculated from flux linkage derivatives $d\boldsymbol{\psi}/dt$ as shown in Fig. 2. The flux linkage derivatives are calculated by taking the resistive voltage drop $\mathbf{R}\mathbf{i}$ and induced voltage $\omega\boldsymbol{\psi}$ away from the input terminal voltage \mathbf{u} as shown in Fig. 3.

1) Incremental Inductance Matrix

The matrix of incremental inductances is the Jacobian matrix of flux linkages

$$\mathbf{l} = \mathbf{J}_{\boldsymbol{\psi}}(i_d, i_q, i_f) = \begin{bmatrix} \frac{\partial \psi_d}{\partial i_d} & \frac{\partial \psi_d}{\partial i_q} & \frac{\partial \psi_d}{\partial i_f} \\ \frac{\partial \psi_q}{\partial i_d} & \frac{\partial \psi_q}{\partial i_q} & \frac{\partial \psi_q}{\partial i_f} \\ \frac{\partial \psi_f}{\partial i_d} & \frac{\partial \psi_f}{\partial i_q} & \frac{\partial \psi_f}{\partial i_f} \end{bmatrix} \quad (15)$$

The flux linkages can be transformed from stator and rotor flux linkages calculated in finite element method (FEM)

$$\boldsymbol{\psi} = \mathbf{T}_{abcf \rightarrow dqf} \boldsymbol{\psi}_{abcf} \quad (16)$$

where

$$\mathbf{T}_{abcf \rightarrow dqf} = \begin{bmatrix} \mathbf{T}_{abc \rightarrow dq} & \mathbf{0}_{2 \times 1} \\ \mathbf{0}_{1 \times 2} & 1 \end{bmatrix}, \quad \boldsymbol{\psi}_{abcf} = \begin{bmatrix} \psi_a \\ \psi_b \\ \psi_c \end{bmatrix} \quad (17)$$

$\mathbf{T}_{abc \rightarrow dq}$ is the transform from abc-frame to dq-frame.

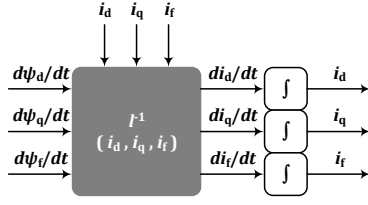


Fig. 2 Calculation of currents in EESM dynamic modeling.

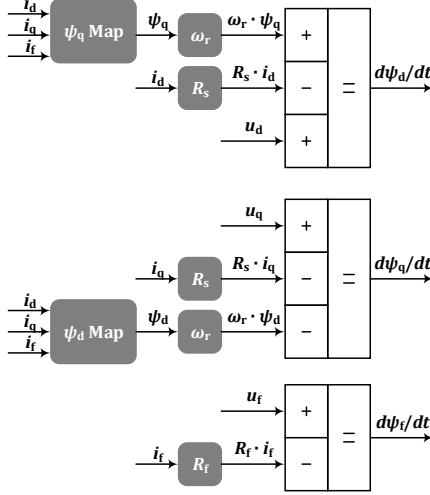


Fig. 3 Calculation of flux linkage derivatives in EESM dynamic modeling.

2) Apparent Inductance Matrix

The apparent inductance between stator and field windings can be calculated from FEM

$$\mathbf{L}_{abcf} = \begin{bmatrix} L_{aa} & L_{ab} & L_{ac} & L_{af} \\ L_{ba} & L_{bb} & L_{bc} & L_{bf} \\ L_{ca} & L_{cb} & L_{cc} & L_{cf} \\ L_{fa} & L_{fb} & L_{fc} & L_{ff} \end{bmatrix} \quad (18)$$

The inductance matrix in dq-frame \mathbf{L} can be transformed from the inductance matrix in abc-frame

$$\mathbf{L} = \mathbf{T}_{abcf \rightarrow dqf} \mathbf{L}_{abcf} \mathbf{T}_{dqf \rightarrow abcf} \quad (19)$$

where

$$\mathbf{T}_{dqf \rightarrow abcf} = \begin{bmatrix} \mathbf{T}_{dq \rightarrow abc} & \mathbf{0}_{3 \times 1} \\ \mathbf{0}_{1 \times 3} & 1 \end{bmatrix} \quad (20)$$

$\mathbf{T}_{dq \rightarrow abc}$ is the transform from dq-frame to abc-frame.

III. DYNAMIC CURRENT CONTROL

The dynamic current control scheme applied in this study is the one presented in [17]. The aim of the dynamic current control is to decouple the d-axis, q-axis and field currents, so that the machine can be regarded as a stacking of three single-input single-output (SISO) systems.

To achieve this, the controller output voltage can be decomposed into three parts, the voltage across the resistances and self-inductances \mathbf{u}_{self} , the voltage across the mutual-inductances $\mathbf{u}_{\text{mutual}}$, and cross-coupling part $\mathbf{u}_{\text{cross}}$

$$\mathbf{u} = \mathbf{u}_{\text{self}} + \mathbf{u}_{\text{mutual}} + \mathbf{u}_{\text{cross}} \quad (21)$$

In \mathbf{u}_{self} , the d-axis, q-axis and field circuits are considered as independent

$$\mathbf{u}_{\text{self}} = \mathbf{l}_{\text{self}} \frac{d\mathbf{i}}{dt} + \mathbf{R}\mathbf{i} = \mathbf{K}_p \mathbf{i}_{\text{err}} + \mathbf{K}_I \int \mathbf{i}_{\text{err}} dt \quad (22)$$

where \mathbf{l}_{self} is the self-inductance matrix

$$\mathbf{l}_{\text{self}} = \begin{bmatrix} l_{dd} & 0 & 0 \\ 0 & l_{qq} & 0 \\ 0 & 0 & l_{ff} \end{bmatrix} \quad (23)$$

\mathbf{i}_{err} is the error current to eliminate

$$\mathbf{i}_{\text{err}} = \mathbf{i}_{\text{ref}} - \mathbf{i}_{\text{msr}} \quad (24)$$

\mathbf{K}_p and \mathbf{K}_I are matrices of PI coefficients

$$\mathbf{K}_p = \alpha_c \mathbf{L}, \quad \mathbf{K}_I = \alpha_c \mathbf{R} \quad (25)$$

\mathbf{A}_c is the matrix of control bandwidth

$$\alpha_c = \begin{bmatrix} \alpha_{c,d} & 0 & 0 \\ 0 & \alpha_{c,q} & 0 \\ 0 & 0 & \alpha_{c,f} \end{bmatrix} \quad (26)$$

The relation between the bandwidth α_c in rad/s and risetime t_r in s follows

$$t_r = \ln 9 / \alpha_c \quad (27)$$

To have a first-order response, the PI coefficients are set as

$$k_p = \alpha_c \cdot L, \quad k_i = \alpha_c \cdot R \quad (28)$$

In $\mathbf{u}_{\text{mutual}}$, the d-axis voltage is decided by the q-axis and field current derivatives, the q-axis voltage is decided by the d-axis and field current derivatives and the field voltage is decided by the d-axis and q-axis current derivatives

$$\mathbf{u}_{\text{mutual}} = \mathbf{l}_{\text{mutual}} \frac{d\mathbf{i}}{dt} \quad (29)$$

where $\mathbf{l}_{\text{mutual}}$ is the mutual inductance matrix

$$\mathbf{l}_{\text{mutual}} = \begin{bmatrix} 0 & l_{dq} & l_{df} \\ l_{qd} & 0 & l_{qf} \\ l_{fd} & l_{fq} & 0 \end{bmatrix} \quad (30)$$

The cross-coupling part $\mathbf{u}_{\text{cross}}$ is feedforward of the EMF induced in each winding

$$\mathbf{u}_{\text{cross}} = \omega \boldsymbol{\psi} = \omega \mathbf{L} \mathbf{i} \quad (31)$$

IV. OBSERVATION OF FIELD CURRENT AND TEMPERATURE

The idea of an observer is to have a machine model running in parallel with the real machine. The machine states, i.e. i_d , i_q and i_f , are predicted based on the machine model while the accessible outputs of the real machine, i.e. i_d and i_q , are measured. Errors between the predictions and measurements of the accessible states are calculated. The errors are then fed back to correct the prediction. The schematic diagram of current estimation is shown in Fig. 4.

The correction vector is to tune the slope of current rise so that the corrected vector shows where the actual current should be. This correction implies the error of prediction due to the field winding resistance. Hence the information of how much and in which direction should field winding resistance be adjusted can be extracted. Since the estimation of winding temperature is based on current estimation, a machine thermal model is not needed. When the field winding temperature increases, the field current will decrease, and the winding temperature estimation will be adjusted accordingly.

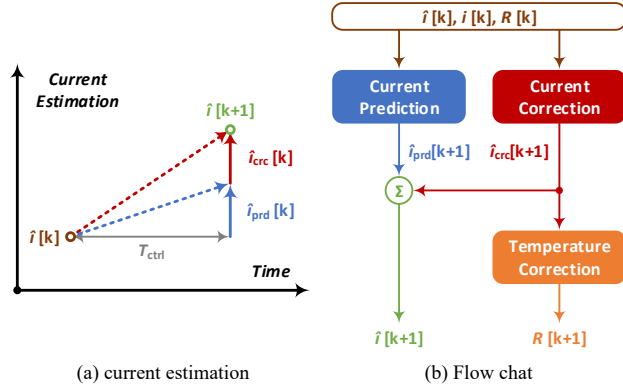


Fig. 4 field current and field winding temperature estimations.

A. Discretization of Electrical Dynamics

The continuous dynamics in (10) can be discretized as

$$\mathbf{i}[k+1] = \mathbf{A}_d \mathbf{i}[k] + \mathbf{B} \mathbf{u}[k] + \mathbf{F} \mathbf{v}[k] \quad (32)$$

where \mathbf{A}_d is the discretized dynamic matrix of \mathbf{A} with control discretization time step T_{ctrl}

$$\mathbf{A}_d = e^{\mathbf{A}T_{\text{ctrl}}} \quad (33)$$

and $\mathbf{F} \mathbf{v}[k]$ describes the process noise.

The output equation in (13) can be discretized as

$$\mathbf{y}[k] = \mathbf{C} \mathbf{i}[k] + \mathbf{w}[k] \quad (34)$$

where $\mathbf{w}[k]$ describes the measurement noise

B. Observation of Field Current

The observation of system states is in two steps. The first step is to predict the current by using the dynamic model. The second step is to correct the prediction using the error between the measured outputs and the predicted outputs.

$$\hat{\mathbf{i}}[k+1] = \hat{\mathbf{i}}_{\text{prd}}[k+1] + \hat{\mathbf{i}}_{\text{crc}}[k+1] \quad (35)$$

In this study, Kalman Filter is adopted as the state observer since it is well-known and already commonly used. However, this is just an example. Other types of observers shall still work providing the same prediction-correction mechanism is used. The prediction and can be described as

$$\hat{\mathbf{i}}_{\text{prd}}[k+1] = \mathbf{A}_d \hat{\mathbf{i}}[k] + \mathbf{B} \mathbf{u}[k] \quad (36)$$

The correction can be described as

$$\hat{\mathbf{i}}_{\text{crc}}[k+1] = \mathbf{K}[k](\mathbf{y}[k] - \mathbf{C} \hat{\mathbf{i}}[k]) \quad (37)$$

where \mathbf{K} is the correction matrix

$$\mathbf{K}[k] = \mathbf{A}_d \mathbf{P}[k] \mathbf{C}^T (\mathbf{R}_w + \mathbf{C} \mathbf{P}[k] \mathbf{C}^T)^{-1} \quad (38)$$

and \mathbf{P} is the error covariance

$$\mathbf{P}[k] = \mathbf{E}\{(\mathbf{i}[k] - \hat{\mathbf{i}}[k])(\mathbf{i}[k] - \hat{\mathbf{i}}[k])^T\} \quad (39)$$

The error covariance \mathbf{P} can be estimated as

$$\mathbf{P}[k] = (\mathbf{A} - \mathbf{K}[k] \mathbf{C}) \mathbf{P}[k-1] (\mathbf{A} - \mathbf{K}[k] \mathbf{C})^T + \mathbf{Q}[k] \quad (40)$$

where

$$\mathbf{Q}[k] = \mathbf{F} \mathbf{R}_v \mathbf{F}^T + \mathbf{K}[k] \mathbf{R}_w \mathbf{K}^T[k] \quad (41)$$

The initial error covariance is zero.

C. Observation of Field Winding Temperature

The correction vector calculated in (37) compensates for the mismatch between the predicted stator currents and the measured stator currents. This mismatch is due to two

reasons: (1) the discretization error of the dynamic system; (2) the error of field winding resistance in the prediction step.

The first error is at higher frequency since such error occurs at each discretization step. The second error is at lower frequency since the resistance change is due to temperature and temperature changes much slower than the discretization frequency. To separate them, a first-order infinite impulse response (IIR) low pass filter can be applied

$$H(z) = (1 - e^{-\omega_c T_{\text{ctrl}}}) / (z - e^{-\omega_c T_{\text{ctrl}}}) \quad (42)$$

where ω_c is the cutoff frequency.

After the low frequency component is extracted, the correction vector $\hat{\mathbf{i}}_{\text{crc}}$ can be used to calculate how much voltages across inductances are missing. The missing voltages is caused by error in resistance in prediction step

$$\mathbf{li}_{\text{crc}}[k+1] = \tilde{\mathbf{R}}[k] \mathbf{i}[k] \quad (43)$$

where $\tilde{\mathbf{R}}$ is the estimation error of resistance. Thus the direction and amount of resistance tuning are implied. In this study, the tuning of resistance is proportional to the estimation error of resistance

$$\hat{R}_f[k+1] = \hat{R}_f[k] + k_R \tilde{R}_f[k] \quad (44)$$

where k_R is a proportional scaling factor. The estimated resistance is then used to calculate the winding temperature

$$\Delta \hat{T}_f[k] = k_R \tilde{R}_f[k] / \rho_{\text{Cu}} / R_{f@100^\circ\text{C}} \quad (45)$$

V. PERFORMANCE EVALUATION

A. Machine and Converter

To evaluate the performance, the 8-pole 48-slot EESM designed in [18] is considered. The machine is designed with the assistance of Ansys Maxwell. The maximum current densities in stator and windings are 15 A/mm² and 10 A/mm². The distributions of flux density at no load and peak torque are shown in Fig. 5. The machine parameters are listed in TABLE I.

The flux linkages in d- and q-axis at different field excitation levels are shown in Fig. 6. As the field current increases, the patterns of ψ_d and ψ_q shift to the left gradually. The curved contours show clear evidence of cross-saturation, i.e., I_d affects the distribution of ψ_q and I_q affects that of ψ_d . Apparent inductances L_{dd} and L_{qq} at zero dq currents are shown in Fig. 7 as field current increases. Saturation can be clearly observed.

There are two power electronic converters used in this study. A three-phase inverter delivers power to the stator winding while a dc-dc H-bridge converter delivers power to the field winding. These two converters share the same dc-link voltage source. Since the focus of this study is the control aspect of the machine, the converters here are considered as ideal voltage sources without voltage drops across the switches or the transformer of the H-bridge converter. The switching actions of the converters are modeled as the averaged voltage level during the entire switching cycle. The parameters of the converters are listed in TABLE II. The voltage limit of the three-phase inverter is decided by considering only the linear modulation range. In this study, the machine model and control algorithm are implemented in Simulink.

TABLE I
MACHINE PARAMETERS

Parameter	Symbol	Value	Unit
lamination outer diameter	$d_{s,outer}$	270	mm
lamination stack length	L_{stack}	360	mm
peak torque	$T_{em,max}$	800	N·m
peak power	$P_{em,max}$	250	kW
maximum stator current amplitude	$I_{s,amp,max}$	450	A
maximum field current	$I_{f,max}$	7.854	A
stator resistance @ 100°C	R_s	19.55	mΩ
field resistance @ 100°C	R_f	54.71	Ω
d-axis self-inductance @ zero current	L_{dd-0}	1.3	mH
q-axis self-inductance @ zero current	L_{qq-0}	1.3	mH
field self-inductance @ zero current	L_{ff-0}	141	H
df mutual -inductance @ zero current	l_{df-0}	52	mH

TABLE II
POWER ELECTRONIC CONVERTERS

Parameters	Symbol	Value	Unit
dc-link voltage	U_{dc}	800	V
H-bridge converter transformer turns ratio	α_T	1:1	
three-phase inverter switching frequency	$f_{sw,3\phi}$	20	kHz
H-bridge inverter switching frequency	$f_{sw,H}$	100	kHz

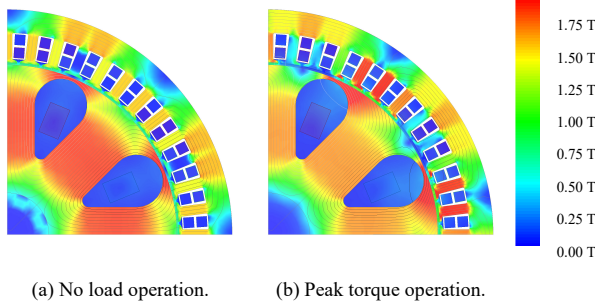


Fig. 5 Flux density distribution.

B. Field Current Observation

Firstly, the observation of field current is evaluated to check if the correction mechanism is able to eliminate the prediction error due to the error in field winding temperature. Hence, temporarily, (1) the field winding temperature update in observer is deactivated, and (2) the measured currents, instead of the estimated currents, are used as the feedback to the current controller.

To evaluate the prediction and correction mechanism, the armature (stator) winding temperature in the observer is the real value, 100°C, whereas the field (rotor) winding temperature in the observer is set at 25°C while the real temperature is 100°C. A comparison between prediction only and prediction together with correction is made and presented in Fig. 8 and Fig. 9.

As can be noticed in Fig. 8, with the temperature error, the predictions of d-axis current and field current diverge from the measurements significantly, while the q-axis current does not. This is probably due to the strong magnetic coupling between the d-axis stator winding and field winding in the flux path. If one current is predicted incorrectly, so will the other. However, the mutual coupling between the d-axis and

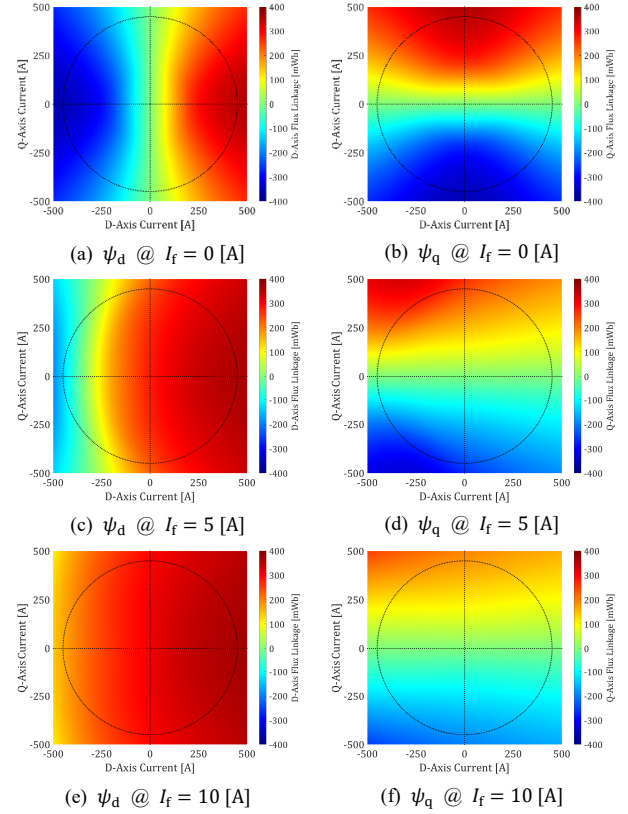


Fig. 6 Flux linkages in d- and q-axis at different field excitation levels.

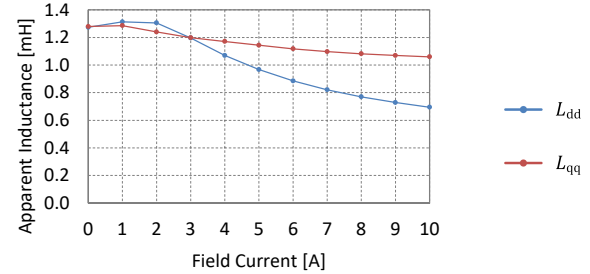


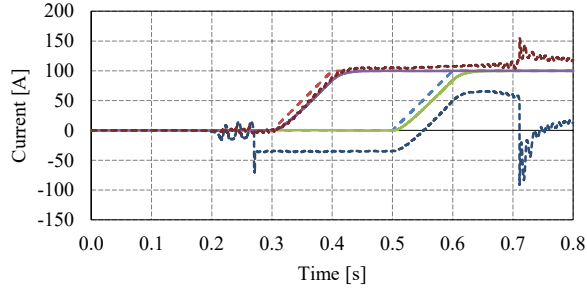
Fig. 7 Apparent inductances L_{dd} and L_{qq} as field current increases. q-axis is much weaker. This is why the prediction of q-axis current is less affected. This also indicates that the prediction works, but it only works with little parameter error.

After the correction step in (37) is added, the performance is presented in Fig. 9. As can be noticed, the errors in predictions are eliminated and the estimations closely follow the measurements. This proves the effectiveness of the correction mechanism.

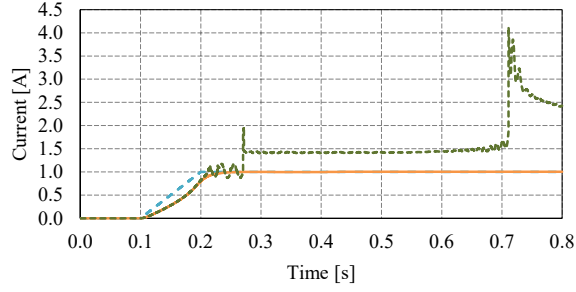
The trace of temperature adjustment value $\Delta\hat{T}_f$ is presented in Fig. 10. Again, this trace is not fed to the observer to correct the resistance. It is only used to interpret the response of the adjustment mechanism. This factor k_R is selected as 100 which is quite arbitrary in this case. The general rules to select a proper k_R will be explained after the correction of resistance is activated. As can be seen, the temperature adjustment appears during the increase of field current. This shows that the temperature error is detected using (42)-(45). After the field current comes to steady state, the adjustment finishes.

C. Field Winding Temperature Observation

Now the temperature correction using (42)-(45) is used to update the resistance value in the observer. Minor difference can be noticed comparing response of current estimation in

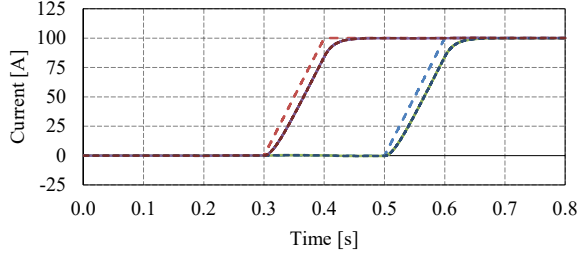


(a) Prediction of d- and q-axis currents.

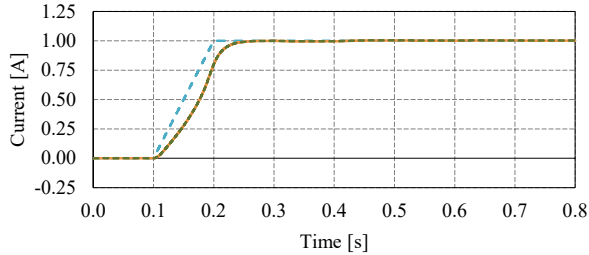


(b) Prediction of field current.

Fig. 8 Estimation of currents with prediction only.



(a) Estimation of d- and q-axis currents.



(b) Estimation of field current.

Fig. 9 Estimation of currents with prediction and correction.

this scenario to Fig. 9, so the curves are not presented here. This indicates that the temperature update does not disturb the observation of currents. The temperature adjustment value is presented in Fig. 11 and the estimated temperature of field winding is presented in Fig. 12. Comparing Fig. 10 and Fig. 11, it can be found out that as the temperature is being corrected, the temperature adjustment value $\Delta\hat{T}_f$ decreases swiftly. As a result, the temperature estimation tracks the real winding temperature in the machine as shown in Fig. 12. 90% of the estimation error is eliminated within 20 ms. The general rules to select a proper k_R are that (1) it should be high enough to damp any possible spikes, especially in the beginning of the current rise; (2) it should be low enough to make sure that the correction of field winding resistance is significant enough so that it ends before the correction of field current finishes, as presented in Fig. 10, because in this algorithm, the correction of field winding resistance relies on the correction of field current. This indicates that with this algorithm, errors can only be corrected when current flows.

D. Dynamic Current Control with Observer

In the end, the estimated field current is fed back to the current controller input. Minor difference can be detected when comparing the current estimation performance to Fig. 9 and the temperature tracking performance to Fig. 12. This means that the observation of field current and temperature is successful in dynamic current control of the machine.

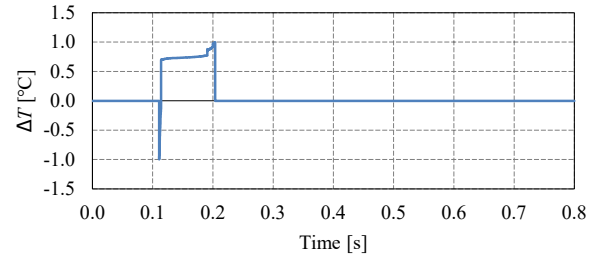


Fig. 10 Temperature adjustment value $\Delta\hat{T}_f$ with prediction and correction.

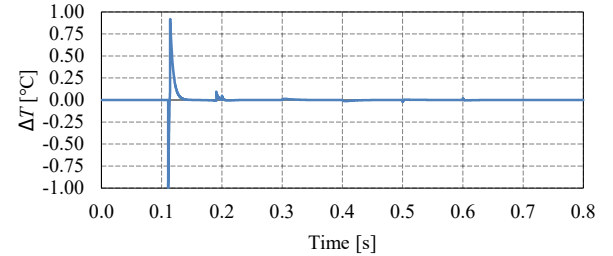


Fig. 11 Temperature adjustment value $\Delta\hat{T}_f$ when the update is activated.

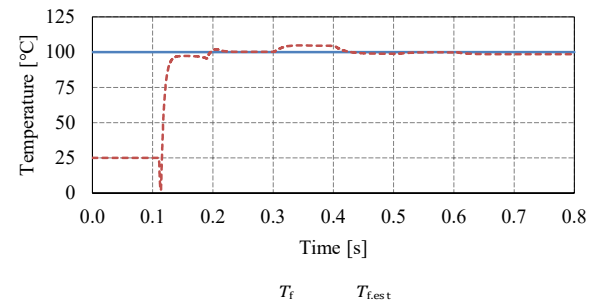


Fig. 12 Temperature estimation of field winding.

VI. CONCLUSIONS

In this study, an algorithm is proposed to observe the field current and field winding temperature of an EESM with brushless excitation. The current observation is constructed in two steps: prediction and correction. The correction step of Kalman filter is adopted as an example. The amount of correction calculated indicates the error in prediction step. This error is due to the incorrect field winding resistance value used in prediction. The correction value is then interpreted and used to adjust the field winding resistance. The adjustment of field winding resistance is then converted to the adjustment of field winding temperature. The algorithm is evaluated in simulations. The estimated field current follows the measurement closely and the tracking of field winding temperature works well. This shows the success of the observation of field current and field winding temperature in electrically excited synchronous machines with brushless excitation.

VII. REFERENCES

- [1] E. M. Illiano, "Design of a Highly Efficient Brushless Current Excited Synchronous Motor for Automotive Purposes," Swiss Federal Institute of Technology in Zurich (ETH Zurich), Zurich, 2014.
- [2] E. M. Illiano, "Design of a Brushless Separately Excited Synchronous Motor," BRUSA Elektronik AG, Sennwald, 2014.
- [3] Green Car Congress, "BMW iX, i4 Gran Coupé EVs to make North American debuts in LA on 1 June," Green Car Congress, 18 May 2021. [Online]. Available: <https://www.greencarcongress.com/2021/05/20210518-bmw.html>. [Accessed 20 March 2022].
- [4] Green Car Congress, "BMW iX M60 features newly developed, high-power density 489 hp synchronous motor; 2.59 kW/kg," Green Car Congress, 05 January 2022. [Online]. Available: <https://www.greencarcongress.com/2022/01/20220105-ix60.html>. [Accessed 20 March 2022].
- [5] MAHLE, "MAHLE develops highly efficient magnet-free electric motor," MAHLE, 05 May 2021. [Online]. Available: <https://www.mahle.com/en/news-and-press/press-releases/mahle-develops-highly-efficient-magnet-free-electric-motor--82368>. [Accessed 20 03 2022].
- [6] D. G. Dorrell, A. M. Knight, M. Popescu, L. Evans and D. A. Staton, "Comparison of Different Motor Design Drives for Hybrid Electric Vehicles," in 2010 IEEE Energy Conversion Congress and Exposition, Atlanta, 2010.
- [7] J. D. Widmer, R. Martin and M. Kimiabeigi, "Electric Vehicle Traction Motors without Rare Earth Magnets," Sustainable Materials and Technologies, vol. 3, pp. 7-13, 2015.
- [8] K. Binnemans, P. T. Jones, B. Blanpain, T. V. Gerven, Y. Yang, A. Walton and M. Buchert, "Recycling of Rare Earths: A Critical Review," Journal of Cleaner Production, vol. 51, pp. 1-22, 2013.
- [9] R. Wang, S. Pekarek and M. Bash, "Alternative excitation strategies for a wound rotor synchronous machine drive," in 2012 IEEE Energy Conversion Congress and Exposition (ECCE), Raleigh, NC, USA, 2012.
- [10] K. Liang, W. Xuhui and F. Tao, "A new method to plan the optimal field excitation current trajectory in a hybrid excitation machine," in 2011 International Conference on Electrical Machines and Systems (ICEMS), Beijing, China, 2011.
- [11] L. Huang, Z. Zhu and W. Chu, "Optimization of Electrically Excited Synchronous Machine for Electrical Vehicle Applications," in Machines and Drives (PEMD 2016), 8th IET International Conference on Power Electronics, Glasgow, UK, 2016.
- [12] J. Tang and Y. Liu, "Design and Experimental Verification of a 48 V 20 kW Electrically Excited Synchronous Machine for Mild Hybrid Vehicles," in 2018 XIII International Conference on Electrical Machines (ICEM), Alexandroupoli, 2018.
- [13] Y. Kim and K. Nam, "Copper-Loss-Minimizing Field Current Control Scheme for Wound Synchronous Machines," IEEE Transactions on Power Electronics, vol. 32, no. 2, pp. 1335 - 1345, 2017.

- [14] C. Stancu, T. Ward, K. M. Rahman, R. Dawsey and P. Savagian, "Separately Excited Synchronous Motor With Rotary Transformer for Hybrid Vehicle Application," IEEE Transactions on Industry Applications, vol. 54, no. 1, pp. 223-232, 2018.
- [15] A. D. Gioia, I. P. Brown, Y. Nie, R. Knippel, D. C. Ludois, J. Dai, S. Hagen and C. Altheld, "Design and Demonstration of a Wound Field Synchronous Machine for Electric Vehicle Traction With Brushless Capacitive Field Excitation," IEEE Transactions on Industry Applications, vol. 54, no. 2, pp. 1390 - 1403, 2018.
- [16] J. Tang, Y. Liu and S. Lundberg, "Estimation Algorithm for Current and Temperature of Field Winding in Electrically Excited Synchronous Machines With High-Frequency Brushless Exciters," IEEE Transactions on Power Electronics, vol. 36, no. 3, pp. 3512 - 3523, 2021.
- [17] J. Tang and Y. Liu, "Dynamic Current Control to Compensate for Magnetic Mutual Coupling in Electrically Excited Synchronous Machines," in 2020 International Conference on Electrical Machines (ICEM), Gothenburg, Sweden, 2020.
- [18] J. Tang and Y. Liu, "Design of Electrically Excited Synchronous Machines to Achieve Unity Power Factor in Field Weakening for Long-Haul Electric Trucks," in 2020 International Conference on Electrical Machines (ICEM), Gothenburg, 2020.

VIII. BIOGRAPHIES

Junfei Tang (S'16-M'22) received the B.Eng. degree in electrical engineering from Jiangsu University, Zhenjiang, China, in 2013, and the M.Sc and Ph.D degrees in electric power engineering from Chalmers University of Technology, Gothenburg, Sweden, in 2016 and 2021 respectively. Now he is a postdoctoral researcher in electric machines and power electronics in Chalmers University of Technology. Junfei Tang was acknowledged as a star reviewer for 2020 by the IEEE Power & Energy Society and the Editorial Board of the IEEE Transactions on Energy Conversion.

Luca Boscaglia (S'17-M'19) received his B.Sc. and M.Sc. in electrical engineering respectively from University of Napoli Federico II and Politecnico di Torino, in Italy. He did his master thesis at ABB Traction Motors in Västerås, Sweden, about thermal and CFD modeling of electric traction motors for railway. He joined ABB Low Voltage Motors and Generators in Vittuone in 2019, in Milan, working in R&D mostly on thermal design and fluid dynamic computations of electrical machines. In 2020, he started the PhD at Chalmers University of Technology in Göteborg, Sweden, on Electrical Machine Design for Vehicle Applications.

Bowen Jiang (S'21) received the M.Sc. degree in automotive engineering from Chalmers University of Technology, Gothenburg, Sweden, in 2020. He is currently pursuing the Ph.D. degree in electrical engineering at Chalmers University of Technology, Gothenburg, Sweden. His current research interests include electric machine control and battery management system algorithms for electric vehicle applications.

Hao Chen (M'19) received the B.Sc. degree in electrical engineering from the School of Electrical Engineering, Beijing Jiaotong University, Beijing, China, in 2012, and the Ph.D. degree in control science and engineering from the School of Automation, Beijing Institute of Technology, Beijing, China, in 2019. From 2016 to 2018, he was with the Department of Electrical and Computer Engineering, Marquette University, Milwaukee, WI, USA, as a Joint Ph.D. Student. From 2019 to 2021, he was a Postdoctoral Research Fellow with the School of Electrical and Electronic Engineering, Nanyang Technological University, Singapore. He is currently a Researcher with the Department of Electrical Engineering, Chalmers University of Technology, Gothenburg, Sweden. His research interests include the design and optimization of electric machines, power electronic drives, and motor control.

Yujing Liu (SM'12) received B.Sc., M.Sc. and Ph.D. degrees in electrical engineering from Harbin Institute of Technology, Harbin, China, in 1982, 1985, and 1988, respectively. In 1996-2013, he worked in ABB Corporate Research, Västerås, Sweden. Since 2013, he is a professor on electrical power engineering in Chalmers University of Technology, Gothenburg, Sweden. His interest includes research on motors, converters, and wireless charging for electric vehicles, generators and power electronics for tidal power conversion, and high efficiency machines for energy saving in industrial applications. Yujing Liu is a senior IEEE member and a member in Swedish Standard Committee on Electrical Machines.